Interpreting Crab Nebula's synchrotron spectrum: two acceleration mechanisms

Maxim Lyutikov,[1]⋆ Tea Temim,[2] Sergey Komissarov ,[3] Patrick Slane,[4] Lorenzo Sironi[5] and Luca Comisso[5]

[1]*Department of Physics and Astronomy, Purdue University, 525 Northwestern Avenue, West Lafayette, IN 47907, USA*
[2]*Space Telescope Science Institute, 3700 San Martin Drive, Baltimore, MD 21218, USA*
[3]*School of Mathematics, University of Leeds, LS29JT Leeds, UK*
[4]*Harvard-Smithsonian Center for Astrophysics, 60 Garden St., Cambridge, MA 02138, USA*
[5]*Department of Astronomy, Columbia University, 550 W 120th St, New York, NY 10027, USA*

ABSTRACT

We outline a model of the Crab pulsar wind nebula with two different populations of synchrotron emitting particles, arising from two different acceleration mechanisms: (i) Component-I due to Fermi-I acceleration at the equatorial portion of the termination shock, with particle spectral index $p_I \approx 2.2$ above the injection break corresponding to $\gamma_{wind}\sigma_{wind} \sim 10^5$, peaking in the ultraviolet (UV, $\gamma_{wind} \sim 10^2$ is the bulk Lorentz factor of the wind, $\sigma_{wind} \sim 10^3$ is wind magnetization); and (ii) Component-II due to acceleration at reconnection layers in the bulk of the turbulent Nebula, with particle index $p_{II} \approx 1.6$. The model requires relatively slow but highly magnetized wind. For both components, the overall cooling break is in the infrared at ~ 0.01 eV, so that the Component-I is in the fast cooling regime (cooling frequency below the peak frequency). In the optical band, Component-I produces emission with the cooling spectral index of $\alpha_o \approx 0.5$, softening towards the edges due to radiative losses. Above the cooling break, in the optical, UV, and X-rays, Component-I mostly overwhelms Component-II. We hypothesize that acceleration at large-scale current sheets in the turbulent nebula (Component-II) extends to the synchrotron burn-off limit of $\epsilon_s \sim 100$ MeV. Thus in our model acceleration in turbulent reconnection (Component-II) can produce both hard radio spectra and occasional gamma-ray flares. This model may be applicable to a broader class of high-energy astrophysical objects, like active galactic nuclei and gamma-ray burst jets, where often radio electrons form a different population from the high-energy electrons.

Key words: pulsars: Individual: Crab – radiation mechanisms: nonthermal.

1 INTRODUCTION

The Crab Nebula is the paragon of the high-energy astrophysical source. Understanding physical processes operating in the Crab has enormous implications for high-energy astrophysics in general. Conventionally, the particle acceleration was assumed to occur at the wind termination shocks, presumably via the Fermi-I mechanism (Rees & Gunn 1974; Kennel & Coroniti 1984a,b). The expected particle spectral index $p = 2.2$–2.4 (e.g. Blandford & Eichler 1987) matches nicely the inferred non-thermal X-ray synchrotron spectrum, see Section 2 and Fig. 1. (We adopt the notations for the spectral energy distribution (SED) as $F_\nu \propto \nu^{-\alpha}$, and particle energy distribution $f(\gamma) \propto \gamma^{-p}$.)

A strong argument in favour of particle acceleration at the (equatorial part of the) termination shock comes from the fact that the low magnetization numerical models of the Crab Nebula (Komissarov & Lyubarsky 2004; Del Zanna, Amato & Bucciantini 2004) are able to reproduce the morphological details of the Crab Nebula down to intricate details. Until recently, acceleration at the termination shock was the dominant paradigm (Rees & Gunn 1974; Kennel & Coroniti 1984a,b). Consistent with this picture is the fact that low-sigma shocks are efficient particle accelerators (Sironi & Spitkovsky 2011b; Sironi, Spitkovsky & Arons 2013).

One of the biggest problems, recognized by Kennel & Coroniti (1984b), was the radio emission of the Crab and other pulsar wind nebulae (PWNe). First, the radio spectra of PWNe are very hard, with the spectral index α approaching zero in some cases (Reynolds 2001; Green 2014; Reynolds et al. 2017). The implied particle spectral index p is then approaching $p \rightarrow 1$. The spectral index
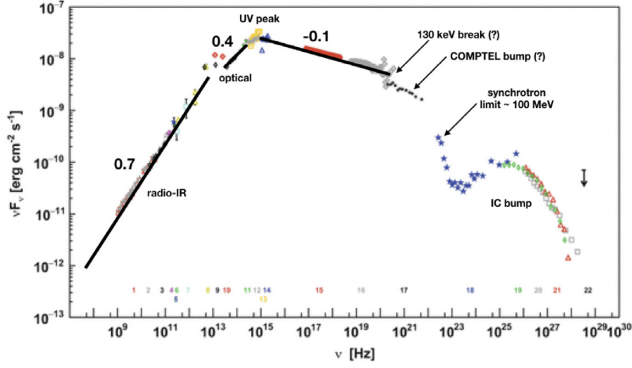
⋆ E-mail: lyutikov@purdue.edu

Figure 1. Broad-band spectrum of the Crab Nebula, reprinted from Zanin (2017). The IR points shown are contaminated by dust emission. We highlighted some features of the spectrum; and numbers indicate scaling of νF_ν with frequency. See the text for details.

$p < 2$ is not expected in Fermi-I acceleration models that typically have $p \geq 2$ (e.g. Blandford & Eichler 1987). Secondly, the number of radio emitting particles is much larger than what is expected in magnetospheric pair production (Kennel & Coroniti 1984b; Atoyan 1999a; Arons & Scharlemann 1979; Timokhin 2010), see also Section 4.3. (We suggest a way to obtain a hard spectrum, but the multiplicity problem remains.)

Another important observation that constrained the structure of PWNe was the discovery of flares from the Crab Nebula (Tavani et al. 2011; Abdo et al. 2011; Weisskopf et al. 2013), which further challenged our understanding of particle acceleration in the PWNe. The unusually short durations, high luminosities, and high photon energies of the Crab Nebula gamma-ray flares require reconsideration of our basic assumptions about the physical processes responsible for acceleration of (some) high-energy emitting particles in the Crab Nebula, and, possibly in other high-energy astrophysical sources.

Even before the discovery of Crab flares, Lyutikov (2010) argued that the observed cut-off in the synchrotron spectrum of the Crab Nebula at ∼100 MeV in the persistent Crab emission is too high to be consistent with the diffusive shock acceleration. Indeed, balancing electrostatic acceleration in a regular electric field with synchrotron energy losses yields a maximum synchrotron photon energy (de Jager et al. 1996; Lyutikov 2010)

$$\epsilon_{\max} \sim \eta \hbar \frac{mc^3}{e^2} \approx 100\,\eta\ \mathrm{MeV}. \qquad (1)$$

where η is the ratio of electric to magnetic field strengths. Since the high conductivity of astrophysical plasmas ensures that in most circumstances $\eta < 1$, the observed value of the cut-off is right at the very limit. During the gamma-ray flares the cut-off energy approached even higher value of ∼400 MeV, suggesting a different acceleration mechanism (Clausen-Brown & Lyutikov 2012; Cerutti, Uzdensky & Begelman 2012a; Cerutti et al. 2014a, 2013; Lyutikov et al. 2017a,b; Lyutikov, Komissarov & Sironi 2018) – particle acceleration during reconnection events in highly magnetized plasma. In particular, Lyutikov et al. (2017b,a) developed a model of explosive reconnection events, whereby particles are accelerated by a charged-starved electric field during the X-point collapse in relativistically magnetized plasma.

In this paper, we argue that there are two acceleration mechanisms in PWNe (which we call, naturally, Component-I and Component-II): Component-I is due to Fermi-I acceleration at the termination

shock (and just thermalization at some parts of the shock) and Component-II is due to plasma turbulence with self-consistent generation of reconnecting current sheets in the bulk of the Nebula. (Therefore, this scenario is different from the models that invoke turbulence with a pre-existing current sheet; Lazarian & Vishniac 1999). The possibility of having two acceleration mechanisms in PWNe has been suggested by Kennel & Coroniti (1984b) and then further discussed by Atoyan & Aharonian (1996), Bandiera, Neri & Cesaroni (2002), Meyer, Horns & Zechlin (2010), Schweizer et al. (2013), and Porth, Komissarov & Keppens (2014). Of particular relevance are the works of Olmi et al. (2014, 2015) who discussed two particle populations and argued that X-ray emission is produced from particles injected in the equatorial regions, while radio electrons are accelerated in the bulk. These are the underlying assumptions in the present study. Also, Komissarov (2013) suggested that magnetic dissipation in the bulk of the Nebula accelerates particles.

Here, we discuss a more detailed model of the two component structure of the Crab Nebula, concentrating on the broad-band SED and the spatial distribution of the emission in different bands.

2 OVERALL SPECTRUM: OBSERVATIONS

2.1 Mean features of the non-thermal component

A number of authors have made fits to the SED of the Crab Nebula (see e.g. reviews by Zanin 2017; Reynolds et al. 2017). Let us briefly summarize them (see Fig. 1):

(i) In the radio, the spectral index is $\alpha_r = 0.3$ (so that $\nu F_\nu \propto \nu^{0.7}$). It is homogeneous over the Nebula (Bietenholz et al. 1997).

(ii) In the infrared (IR), the situation is complicated – a large thermal component from filaments complicates the analysis, see Section 3.3.

(iii) In the optical, the spectrum softens to $\alpha_o \sim 0.6$ (so that $\nu F_\nu \propto \nu^{0.4}$).

(iv) The overall spectral distribution of νF_ν in the Crab Nebula has a peak in the ultraviolet (UV), at ∼1 eV. Above the peak the spectrum has $\alpha \approx 1.1$

(v) An additional feature present in the hard X-ray spectrum is softening at ∼130 keV, with a corresponding break with $\Delta\alpha = 0.43$ (Meyer et al. 2010, see Section 2.2 for further discussions)

(vi) There is also a claim of a mild spectral bump at above ∼1 MeV (van der Meulen et al. 1998), though this may be due to the low statistics of the early The Imaging Compton Telescope (COMPTEL) data set (Kuiper, private communication; also Section 2.2).

(vii) There is an exponential cut-off around 100 MeV (Abdo et al. 2010).

(viii) A new component appears above 1 GeV, peaking at around 100 GeV (Abdo et al. 2010; Aharonian et al. 2006)

2.2 The COMPTEL break and a bump

There are possibly important features in the high-energy Crab Nebula spectrum that seem to be not given enough attention previously. First, there is a softening at ∼130 keV, with a break with $\Delta\alpha = 0.43$ (Meyer et al. 2010). It is not clear if this feature is actually physically present. In Kuiper et al. (2001, their fig. A.1), there seems to be a factor of 1.5–2 jump between the continuation of ∼100 keV spectrum and COMPTEL points above 1 MeV. This could be due to cross-detector uncertainty (Kuiper, private communication). Yet a distinct difference in spectral slopes between ∼1 and 40 MeV
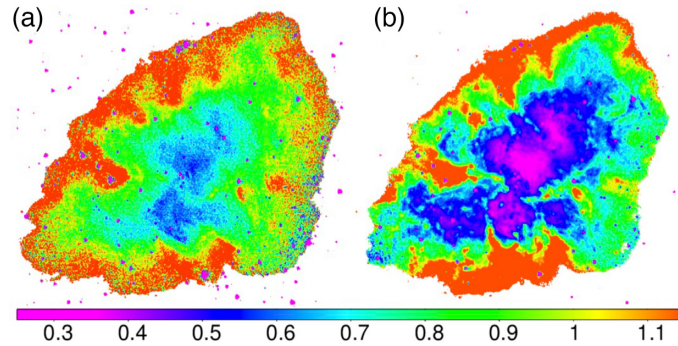
Figure 2. Left-hand panel: map of the spectral index calculated as a difference between the synchrotron-dominated 3.6 and 4.5 μm images. The torus structure is evident in blue, with gradual steeping towards the outer nebula. The uncertainty on the absolute value of the spectral index is estimated to be ±0.3. Right-hand panel: map of the spectral index calculated as a difference between 3.6 and 8.0 μm images. While the presence of the ejecta filaments at 8.0 μm make the spectral index in the outer nebula unreliable, the spectral index for the inner torus seen in magenta is 0.3 ± 0.1. This matches the spectral index of the radio electrons. The colour bars indicate the value of the spectral index.

(van der Meulen et al. 1998) may indicate a different emission component. The data from SPI on *INTEGRAL* (Jourdain & Roques 2009) indicate that a broken power-law spectrum is statistically preferred over a single power law (see fig. 1 in Jourdain & Roques 2009).

Thus, in our model the ∼100 keV–MeV break and the bump arise from a superposition of two components, Section 4.3.5. If confirmed, the COMPTEL break and a bump can be an interesting test of the model. We encourage further analysis of the Crab Nebula data in the MeV range.

3 INTERNAL STRUCTURE - OBSERVATIONS

Above, we discussed the overall properties of the Crab Nebula. Next we highlight important observations related to the internal structure of the Crab Nebula.

3.1 X-rays

X-ray images of the Crab Nebula show interesting morphological variations. At lower energies, 0.5–1.2 keV, the Nebula is considerably more extended than in higher energies. Overall, this is consistent with cooling, though some features (e.g. southward directed elongated feature) are both much brighter in lower energies, and have a corresponding features in radio and IR.

Spectral maps of the Crab in X-rays above 10 keV, i.e. above the *Chandra* band obtained with NuStar, are quite different (see fig. 8 of Madsen et al. 2015; Reynolds et al. 2017). The map of spectral indices indicates that above 10 keV the hardest part is off the main torus, and hardens towards the SE (South-East). This contrasts with the fact that the *Chandra* images show that the high-energy part (up to 7 keV) is nearly all torus. (The effect is not likely due to different spatial resolutions at different energies.)

The morphological map of the X-ray spectral index shows interesting structure: above 10 keV the hardest part is off the main torus, towards the low-left jet (Madsen et al. 2015). The torus spectrum softens sooner (closer to the centre) than the SE part. This can be interpreted as due to the appearance of a new component, Section 3.1.

We interpret the X-ray intensity and spectral maps as follows. The ∼0.1–10 keV intensity is dominated by Component-I; the increasing size of the emission region towards softer energies is due to radiative cooling (X-ray particles have cooling times of the

order of a year). Above 10 keV we start to see Component-II, that eventually produces the COMPTEL bump, Section 2.2.

3.2 Spectral maps in optical: softening towards the edges

The map of the spectral index at optical wavelengths (Veron-Cetty & Woltjer 1993) shows values of α as low as 0.57 in the vicinity of the pulsar with gradual steepening towards the outer edges of the Nebula to values just above unity. The clear softening of the spectrum towards the outer nebula implies that the optical-emitting electrons have cooling times shorter than the age of the Nebula.

3.3 The infrared

As a part of new analysis, we reprocessed the *Spitzer* Infrared Array Camera (IRAC) data originally presented in Temim et al. (2006) using updated calibration files, extended source corrections, and the final v18.5 of the MOPEX (MOsaicker and Point source EXtractor) software. We used the IRAC 3.5, 4.5, and 8.0 μm images from Temim et al. (2006) to create spectral index maps. The images were background subtracted using background levels of 0.18. 0.18, and 8.72 MJy sr^{-1}, respectively. The IRAC surface brightness correction for extended sources was applied to the images (0.91, 0.94, and 0.74, respectively). The images were also corrected for extinction using A_λ/A_K values of Indebetouw et al. (2005) and an A_K value of 0.194, derived from the hydrogen column density towards the Crab Nebula of $N_H = 3.54 \times 10^{21}$ cm^{-2} (Willingale et al. 2001) and the relation $N_H/A_K = 1.821 \times 10^{22}$ cm^{-2} (Draine 1989). This led to extinction correction factors of 1.1 for the 3.6 μm and 1.08 for 4.5 and 8.0 μm images. Finally, we used the nominal wavelengths of 3.550, 4.493, and 7.872 μm to calculate the spectral index maps.

The two IR spectral index maps are shown in Fig. 2. The left-hand panel shows the map calculated from the IRAC 3.6 and 4.5 μm images that are dominated by synchrotron emission. The torus structure, evident in blue, has a spectral index of 0.55. The index steepens with distance from the torus, consistent with previous results. While the relative values of the spectral indices have small uncertainties, the uncertainty on the absolute value of the index for the map on the left is ±0.3, assuming a conservative estimate for the IRAC flux calibration of ∼5 per cent. We therefore produced a second spectral index map using the IRAC 3.6 and 8.0 μm images, which provide larger wavelength spacing and reduce the absolute uncertainty to ±0.1. This map is shown in

the right-hand panel of Fig. 2. Since the IRAC 8.0 μm image has a large contribution from the ejecta filaments, the spectral index is significantly modified in the outer nebula. We can, however, use this map to more reliably constrain the absolute value of the spectral index for the inner torus, which clearly stand out in magenta. Here, the torus has a spectral index of 0.3 ± 0.1. This is consistent with the continuation of the radio spectrum (which is clearly in the regime where radiative losses are not important). Similar spectral indices were found by Gallant & Tuffs (2002) when comparing 16 μm data with Infrared Space Observatory (ISO) from 2 μm.

Fig. 3 shows a deep *Chandra* X-ray image of the Crab Nebula (contours) overlaid with the IR spectral index map from Fig. 2 (left) in magenta. The contours appear to correlate with the morphology of the X-ray emission, both from the inner torus and jet, as well as the fainter regions in the outer nebula. Comparing the spectral maps in the IR with intensities in IR and the X-rays (Fig. 3), we find that there is a correlation, though not a one-to-one correspondence between the IR spectral maps and X-ray intensity contours.

The discussion above describes a complicated picture in the IR. First, there is clear spectral evolution towards the edges both in the optical and the near-IR, indicating that the electrons emitting at these wavelengths also have overall cooling times shorter than the age of the Nebula (Gallant & Tuffs 2002; Temim et al. 2006) (Turbulent mixing may smooth variations of the spectral index Tang & Chevalier 2012; Porth et al. 2016). Second, there is some intensity and spectral correlation with X-rays, but the spectral index in the central part, ~0.3, matches that of the radio emission (this could indicate that we start to see the extension of the radio component).

We interpret these somewhat contradictory facts due to the presence of two emission/acceleration components that produce nearly equal intensities in the IR (Section 6). Previously, Bandiera et al. (2002) argued for two separate distributions, based on significant spatial variations of the spectral index. Gallant & Tuffs (2002) and Temim et al. (2006) found spectral steepening towards the PWN edges, similar to that observed in the optical band.

4 INTERPRETATION OF SPECTRUM: TWO COMPONENTS

4.1 Location and spectra of components

In Fig. 4, we picture various acceleration regions within the Nebula, while in Figs 5 and 6 we outline the particle distributions and the observed spectra.

Qualitatively, there are two components that contribute to the emission; we call them Component-I and Component-II. Component-I is, using the terminology from gamma-ray bursts (GRBs, Sari, Narayan & Piran 1996), in the fast cooling regime: the minimum injection energy corresponds (overall, on the time-scale of the Nebula) to synchrotron emission above the spectral break associated with synchrotron cooling. Component-II is in the slow cooling regime: the injection peak is below the cooling frequency (the higher energy tail of Component-II is still affected by cooling). (Here and below, we use interchangeably the terms the energy of the injected particle and the corresponding energy of the synchrotron photons.)

Our picture for the particle population in the Crab Nebula proposes two distinct components – one (Component-I) injected at low latitudes near the termination shock (corresponding to the Crab torus), and one (Component-II) injected at higher latitudes

and subsequently modified by plasma turbulence with reconnecting current sheets in the bulk of the Nebula. This is illustrated in Fig. 5 where the solid (dashed) curves provide a qualitative description of Component-I (II). Component-I is characterized by a single power law with $dn/d\gamma \propto \gamma^{-p_I}$, while Component-II is assumed to be a broken power law with indices p_{II} and $p_{II, above}$ below and above the injection break at $\gamma_{II, br}$. The black curves represent the spectrum at the time of injection, while the blue curves illustrate the evolved spectra showing breaks introduced by synchrotron cooling.

Thus, an inherent break in Component-II is assumed at injection. As we argue in Section 5.2.5, we expect that particle acceleration in reconnection sheets is sensitive to the average energy per particle in the wind (equation 23). The average energy comes from two components – bulk motion γ_w, and magnetization σ_w. As a result, we expect that Component-II has an injection break at the same energy as the minimal injection energy of the Component-I, $\gamma_{I, min}$, since both lie around the mean energy per particle.

Let us summarize observational evidence, though not conclusive, for the Component-II above the IR:

(i) Indications of a spectral break around 130 keV in the overall spectrum of the Crab (Section 2.2).

(ii) Indications of spectral bump (COMPTEL bump) in the $\geq$ MeV region (Section 2.2).

(iii) The NuStar spectral map above 10 keV shows that the hardest spectra are not correlated with the $\leq$10 keV X-ray torus (Section 3.1). (NuStar sensitivity above 10 keV extends to ~70 keV, so this statement applies to that energy.)

(iv) In IR the spectral index of the central part of the Nebula (~0.3) matches that of the radio photons (Fig. 2).

The associated synchrotron emission from each particle component is illustrated in Fig. 6 where we identify spectral indices and breaks associated with the evolution of the particle spectra, and constrained by observations of the broad-band spectrum of the Crab Nebula. The associated spectral breaks (numbered as in Section 2.1) are (see also Table 1; the numbers given are approximate estimates and may not be unique):

(i) Injection break for Component-II, $\gamma_{min, II}$ (not observed – corresponding synchrotron frequency below ~few tens of MHz).

(ii) *Radio:* the required particle distribution of synchrotron emitting leptons (uncooled Component-II) is $p_{II} = 1 + 2\alpha_r = 1.6$ (by p we mean the injected spectrum).

(iii) *Cooling break in mid-IR:* spectral steepening towards the edges in the optical (Veron-Cetty & Woltjer 1993) and near-IR (Gallant & Tuffs 2002; Temim et al. 2006) indicated that optical and near-IR electrons are in a fast cooling regime – the cooling frequency is in the mid-IR. Particles enter the fast cooling regime, showing steepening towards the edges. The intensity of Component-I sharply drops below the cooling break, where $\nu F_\nu \propto \nu^{4/3}$; above the cooling break Component-I dominates over Component-II.

(iv) In the optical $\alpha_o \approx 0.5$ – these are the electrons from Component-I that were initially emitting in the UV and X-rays, in a fast cooling regime, but cooled down to emit in the optical. In the optical, there is a clear steepening of spectral index towards the edges (Veron-Cetty & Woltjer 1993).

(v) UV peak - $\gamma_{min, I}$ – the peak emission of Component-I. This is the peak energy per particle in the equatorial part of the wind, $\gamma_{min, I} = \gamma_p$.

(vi) We interpret the break at ~130 keV (if it is real) as $\gamma_{max, I} \sim 1.5 \times 10^8$, equation (8), of Component-I. If the claim of the break is not supported by observations, there is no limit on $\gamma_{max, I}$.
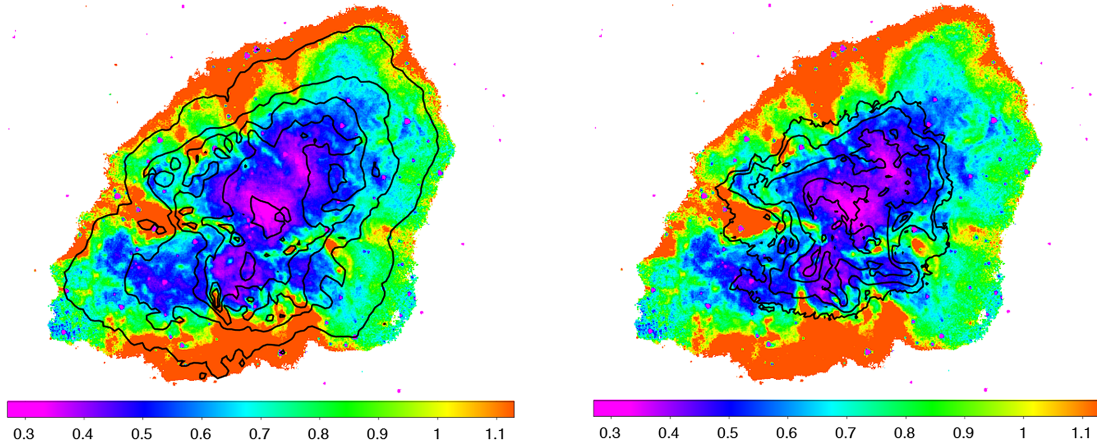
Figure 3. Left-hand panel: the spectral index map from Fig. 2 (calculated as a difference between the synchrotron-dominated 3.6 and 4.5 μm images) overlaid with the contours from the deep *Chandra* X-ray image of the Crab Nebula in black (Seward, Tucker & Fesen 2006). Right-hand panel: the IR spectral index map from Fig. 2 overlaid with the contours from the intensity at 3.6 μm.
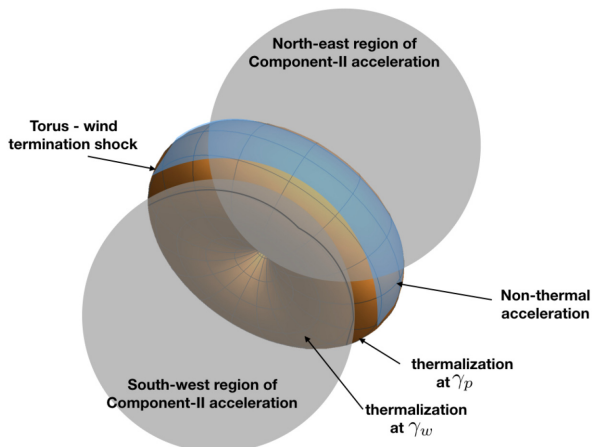

Figure 4. Qualitative picture of various acceleration regions within the Nebula. The wind termination shock is elongated in the equatorial plane. In a limited equatorial sector, the shock produces non-thermal particle spectrum via Fermi-I mechanism (blue stripe), while at intermediate latitudes, the wind is thermalized at $\gamma_p \sim \gamma_w \sigma_w$. These sectors produce Component-I. Since the post-shock flow is mildly relativistic, one also expects NE to SW anisotropy (blue stripe). At higher latitudes, the wind is thermalized at γ_w. In the bulk of the Nebula, closer to the axis (still in the central part), high magnetic field regions form (see white regions in Fig. 7), where plasma turbulence with reconnecting current sheets accelerates Component-II (the south-west is in the font of the torus). The gradient (from NE to SW) in the NuSTAR maps (Madsen et al. 2015; Reynolds et al. 2017) possibly arise due to the fact that the flow immediately post-the-equatorial shock is mildly relativistic – the blue ribbon in is NE-SW asymmetric.

(vii) MeV bump – possible re-appearance of Component-II. (Thus, above few hundred keV, we argue, we start to see the extension of the radio component.) If the MeV bump is not supported by observations, Component-II has a substantial spectral break between IR and X-rays.

(viii) Synchrotron burn-off limit (de Jager et al. 1996; Lyutikov 2010).

(ix) IC component (Atoyan & Aharonian 1996; de Jager et al. 1996).

Thus, our interpretation of the spectrum differs from Kennel & Coroniti (1984b) in one particularly important way: Kennel &
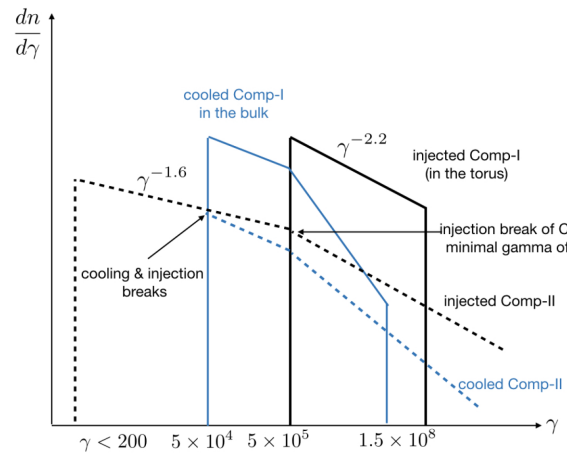

Figure 5. Qualitative picture of two particle distributions. Component-I: solid black line – injected spectrum, solid blue line – cooled spectrum. Component-II: dashed black line – injected spectrum, dashed blue line – cooled spectrum. (Slope of Component-II above the break is not well constrained.) This figure illustrates the initial and eventual spectra for each shell of particles injected into the nebula at some time in the past, not the integral spectra of the components accumulated over the life of the nebula. In addition, spacial variation of the relative intensities are expected.

Coroniti (1984b, see also Bucciantini, Arons & Amato 2011) interpreted the UV break as a cooling break, and the IR break as an injection break. We argue it is the reverse – both IR and optical spectral maps show clear evolution towards the edges, implying that IR and optical electrons have cooling time-scale shorter than the lifetime of the Nebula.

4.2 Component-I

4.2.1 Wind Lorentz factor and magnetization

The Inner Knot in the Crab Nebula – a small bright spot close to the pulsar (Rudy et al. 2015) is interpreted as a surface of the relativistic pulsar wind termination shock (Lyutikov, Komissarov & Porth 2016; Yuan & Blandford 2015). Thus, its properties can be used to probe the properties of the pulsar wind. The Inner Knot is located at intermediate latitudes, ∼45° off the spin axis. Importantly,

Table 1. Properties of the two components.

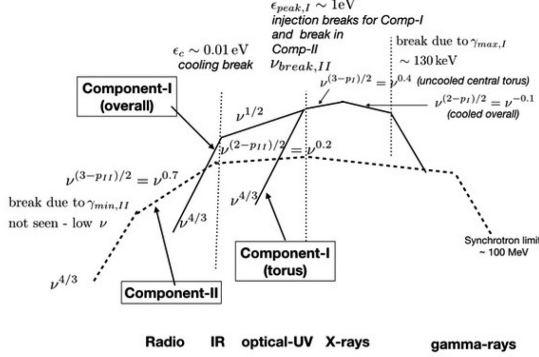| Quantity	Lorentz factor	Photon energy
$\gamma_{\min,\,I}$ – minimal injection for Component-I	$\sim 5 \times 10^5$	$\sim$eV
$\gamma_{\max,\,I}$ – maximal injection for Component-I	$\sim 1.8 \times 10^8$	~ 100 keV
γ_c – cooling energy (both Component-I and Component-II)	$\sim 5 \times 10^4$	~ 0.01 eV
$\gamma_{\min,\,II}$ – minimal injection for Component-II	≤ 200	≤ 100 MHz
$\gamma_{II,\,br} = \gamma_{I,\,min}$ – break in injection spectrum for Component-II	$\sim 5 \times 10^5$	$\sim$eV

Figure 6. Qualitative picture of two synchrotron components in νF_ν. Component-I (solid line) is in the fast cooling regime, with injection energy above the cooling break, while Component-II (dashed line) is in the slow cooling regime. In projection, Component-II partially overlaps with the torus. The spectral breaks are: (i) cooling breaks in both components (ν_c, energy approximately 0.01 eV). [The transition between dashed ($\nu^{0.7}$, Component-II dominated) to solid ($\nu^{0.5}$, Component-I dominated) is not as sharp as is drawn, since the cooling frequency is a very sharp function of the local B-field; plus there is large contribution from dust.] (ii) UV peak – this is $\gamma_{\min,\,I}$ of Component-I (the wind Lorentz factor); (iii) possible 130 keV break due to $\gamma_{\max,\,I}$; (iv) hypothetical break in Component-II somewhere in the UV-soft X-rays – this is required for Component-II not to overshoot Component-I; and (v) Synchrotron emission limit, ~ 100 MeV. It is expected that variations of the magnetic field and of the dynamical times (e.g. in the inner and outer parts of the Nebula) lead to further complications of the picture.

the spectrum of the Inner Knot is thermal, with a peak frequency $\nu_{\mathrm{knot}} \approx$ few times 10^{14} Hz (Porth et al. 2017, though this result has not been confirmed by others yet). The thermal nature of the knot is, first, consistent with the model of Sironi & Spitkovsky (2011b, see also Section 5.1.2) that predicts that the termination shock in the striped wind does not accelerate particles outside of the $\sim \pm 10°$ sector from the equatorial plane. Second, using the model of the post-shock flow developed by Lyutikov et al. (2016), one can estimate the post-shock energy per particle γ_p. Using the peak frequency of the knot emission, and estimates of the post-shock magnetic field and Lorentz factor one finds

$$\gamma_p = \left(\frac{2\pi m_e c \nu_{\mathrm{knot}}}{eB} \right)^{1/2} \approx 5 \times 10^5 b_0^{-1} \quad (2)$$

(Recall that the average energy per particle in the wind consists of the wind Lorentz factor times the magnetization, equation 23). Below we will use the estimate (2) as the minimal $\gamma_{I,\,min}$ for the Component-I.

The peak energy of Component-I is then

$$\epsilon_{p,\,I} \approx \hbar \gamma_p^2 \omega_B = 1.5 b_0 \text{ eV} \quad (3)$$

where $\omega_B = eB/(m_e c)$ is the non-relativistic cyclotron frequency. This matches the observed peak in the Crab spectrum.

The overall cooling break is in the IR:

$$\epsilon_c = \frac{m_e^5 c^9 \hbar}{e^7 B^3 \tau^2} = 10^{-2} b_0^{-3} \text{ eV}, \quad (4)$$

$$\gamma_c = \frac{m_e^3 c^5}{e^4 B^2 \tau} = 5 \times 10^4 b_0^{-2}, \quad (5)$$

where τ is the age of the Nebula.

Note the sharp dependence of ϵ_c and γ_c on the local magnetic field. In a fluctuating field, this will produce large variations in the cooling energy; variations of the magnetic field by a factor of ~ 2 would produce variations in the cooling break of an order of magnitude – the cooling frequency ν_c is expected to vary by at least an order of magnitude between different regions in the Nebula.

Thus, the cooling energy calculated with the age of the Nebula is below the peak energy, $\epsilon_c < \epsilon_{p,\,I}$. According to the terminology of GRBs, this regime ($\epsilon_c \leq \epsilon_p$) is called fast cooling (Sari et al. 1996). In the fast cooling regime,

$$\nu F_\nu \propto \begin{cases} \epsilon^{4/3} & \epsilon < \epsilon_c \\ \epsilon^{1/2} & \epsilon_c < \epsilon < \epsilon_{p,I} \\ \epsilon^{(2-p_I)/2} \propto \epsilon^{-0.1} & \epsilon_{p,I} < \epsilon \end{cases} \quad (6)$$

On the other hand, the inner parts of the Nebula – especially the torus – have dynamical times of few months, and are thus in the slow cooling regime. Thus, we expect for the torus

$$\nu F_\nu \propto \begin{cases} \epsilon^{4/3} & \epsilon < \epsilon_{p,I} \\ \epsilon^{(3-p_I)/2} \propto \epsilon^{0.4} & \epsilon_{p,I} < \epsilon \end{cases} \quad (7)$$

plus a possible exponential break corresponding to $\gamma_{I,\,max}$, and synchrotron limit at ~ 100 MeV or less; in equations (6) and (7), the injection power law is $p_I \approx 2.2$.

If the $\epsilon_b \sim 130$ keV break (Meyer et al. 2010, and Section 2.2) is real, this can be an indication of the maximal acceleration limit of Component-I, $\gamma_{\max,\,I}$:

$$\gamma_{\max,I} = \left(\frac{m_e c \epsilon_b}{e \hbar B} \right)^{1/2} = 1.5 \times 10^8 b_0^{-1/2} \quad (8)$$

4.2.2 The torus: Component-I in slow cooling regime in the central region

In the overall spectrum of the Nebula (Fig. 1), the near-IR flux of few $\times 10^{-8}$ erg cm^{-2} s^{-1} is only mildly lower than in X-rays, $\sim 10^{-8}$ erg cm^{-2} s^{-1}. Yet the torus is barely seen in IR, see Section 3. Thus, the torus emission should decrease sharply below the peak. This can be achieved only if the UV peak is the injection break in the slowly cooling regime[1] – then the slope of νF_ν changes from 4/3 below the peak to $(3 - p_I)/2$ and then to $(2 - p_I)/2$ above the peak.

---

[1] Overall, on the lifetime of the Nebula, Component-I is in the fast cooling regime, while the much smaller torus is in the slow cooling regime.

Consider the immediate post-termination shock region (to be called the 'torus') as a separate entity within a Nebula. Accelerated particles are injected into it (Component-I), they emit, and are advected out by the flow. Thus, the number of emitting particles within the torus region is constant in time (for approximately constant spin-down luminosity). Let us estimate the expected ratio of intensities at two different wavelengths.

As a comparison point, we take X-rays, where the emitting particles are clearly above the injection break and are fast cooling. For frequencies below X-rays, but above the injection break (still in fast cooling), $F_\nu \propto \nu^{-p/2}$. Then comes the UV break at $\nu_{\rm break}$. If it is due to cooling then below it

$$\frac{(\nu F_\nu)_{\rm IR}}{(\nu F_\nu)_{\rm X}} = \left(\frac{\nu}{\nu_{break}}\right)^{(3-p)/2} \left(\frac{\nu_{\rm break}}{\nu_{\rm X}}\right)^{1-p/2} \approx 0.65 \qquad (9)$$

for $h\nu = 0.1$ eV, $h\nu_{\rm break} = 1.5$ eV, $h\nu_{\rm X} = 10^3$ eV, and $p = 2.2$.

Thus, in this case we would expect that the torus is as bright in optical and IR as in X-rays (in terms of surface brightness).

Alternatively, the UV break at $\nu_{\rm break}$ can be due to injection. Then, there are two cases: (i) if the residence time is sufficiently short, so that even particles with $\gamma_{\rm min, I}$ do not experience cooling, then

$$\frac{(\nu F_\nu)_{\rm IR}}{(\nu F_\nu)_{\rm X}} = \left(\frac{\nu}{\nu_{\rm break}}\right)^{4/3} \left(\frac{\nu_{\rm break}}{\nu_{\rm X}}\right)^{1-p/2} \approx 0.05 \qquad (10)$$

Thus, the expected torus brightness in this case is more than an order of magnitude smaller.

(ii) If particles with $\gamma_{\rm min}$ do cool to below the observed frequency, then

$$\frac{(\nu F_\nu)_{\rm IR}}{(\nu F_\nu)_{\rm X}} = \left(\frac{\nu}{\nu_{\rm break}}\right)^{1/2} \left(\frac{\nu_{\rm break}}{\nu_{\rm X}}\right)^{1-p/2} \approx 0.5, \qquad (11)$$

just somewhat smaller than equation (9).

Which of the estimates (10) and (11) is closer to reality? The overall estimate of the cooling break (5) is based on the age of the Nebula. But the inner regions of the Nebula have dynamical times much smaller than the age of the Nebula. As a result, the cooling break for the newly injected particles in the inner parts of the Nebula, in the torus, is at higher energies. Thus, we expect that particles with $\gamma_{\rm min, I}$ will not cool to below (0.1 eV). Hence, estimate (10) is applicable.

These simple theoretical estimates demonstrate that intensity of the torus can decrease precipitously if we identify the UV spectral break with the injection break of Component-I. This then explains the sharp decrease of the torus emissivity from the UV towards the IR.

In principle, this *does not mean* that radio electrons are not accelerated at the termination shock. If a ratio of radio and X-ray emitting electrons within the same volume is $n_{\rm R}/n_{\rm X}$, then in the same magnetic field the ratio of resulting fluxes is

$$\frac{F_{\rm R}}{F_{\rm X}} = \frac{n_{\rm R}}{n_{\rm X}} \frac{\nu_{\rm R}}{\nu_{\rm X}} \qquad (12)$$

Since $\nu_{\rm R}/\nu_{\rm X} \sim 10^{-9}$ – very little emission is expected from the newly injected radio particles: radio-emitting leptons are highly inefficient radiators; the overall radio emission is dominated by the accumulated long-living leptons.

In conclusion, radio electrons may be accelerated at the termination shock, but there is no observational requirement that they *are* accelerated at the termination shock; the shock may not accelerate any radio electrons.

4.2.3 Component-I: energetics

How do Component-I and Component-II compare energetically? Overall, most of the radiative power comes out in the UV, due to Component-I. In our model, the peak UV power of Component-I comes from two related, but somewhat separate components: (i) power-law acceleration by Fermi-I process in the equatorial part, that extends from UV to X-rays – this is energetically the dominant component; and (ii) thermalization at the high latitudes that produce a broad peak in the UV. The power of Component-I is related to the current spin-down power of the pulsar (since Component-I is in the fast cooling regime, most of the energy given to particles at the termination shock is radiated away).

The radiative efficiency of Component-I in case of the Crab is a few per cent. For the wind power $L_{\rm w} \propto \sin^2\theta$ (θ is the polar angle), the amount of wind energy that comes within $\pm 10^\circ$ of the equatorial plane is ~ 25 per cent. Consistent with this estimate, the peak luminosity of Component-I is $L_{\rm p, I} \sim 10^{37}$ erg s^{-1}, see Fig. 1, safely below the spin-down power of the Crab pulsar.

Component-I peaks in the UV at frequencies corresponding to $\gamma_{\rm min, I}$; it cools down to optical–IR over the lifetime of the Nebula. Thus, Component-I is in the fast cooling regime: most of the energy given to the particles during acceleration process is radiated away. To estimate the radiative efficiency of Component-I, we note that the cooling time for the ~ 1 eV injection peak is

$$\tau_{\rm c, peak} = \frac{m_{\rm e}^{5/2} c^{9/2} \sqrt{\hbar}}{e^{7/2} B^{3/2} \sqrt{\epsilon_{\rm p}}} \approx 100\,{\rm yr}\, b_0^{-3/2} \qquad (13)$$

This estimate matches really well the fact that there is a strong spectral evolution in the optical (Veron-Cetty & Woltjer 1993).

The estimate (13) explains the radiative efficiency of the Inner Knot: Lyutikov et al. (2016) found that its radiative efficiency is $\sim 10^{-3}$. Since its spectrum peaks approximately at $\sim$eV (Porth et al. 2017), similar to the peak of the overall spectrum in the Crab, this factor of $\sim 10^{-3}$ is naturally explained as a ratio of the dynamic time of the Knot, $\sim$few months (Rudy et al. 2015), to the cooling time-scale (13). After a few months, the directed post-shock flow loses directionality and becomes turbulent, so that the optical–UV emission is no longer contained within a relatively bright Inner Knot (see Lyutikov et al. 2016, for discussion of how extended is the post-shock emission in the Inner Knot). Importantly, the whole flow contributes to the UV peak of Component-I, not only the equatorial belt where acceleration of X-ray emitting electrons occurs.

In conclusion, the UV peak has cooling time-scale moderately small compared to the age of the Nebula – thus any small feature like the Inner Knot is not very bright. Most of the emission will be distributed. On the other hand, in X-rays, the cooling time-scales are similar to the dynamic time-scales, only a few months, producing sharp features (the X-ray torus).

Overall, the peak intensity in νF_ν of a few per cent seems like a good consistent estimate of the radiative energetics of Component-I.

4.3 Component-II

4.3.1 The spectrum

The emission corresponding to the minimal injection energy of Component-II is very low, below ≤ 100 MHz, so that $\gamma_{\rm p, II} \leq 200$ (the radio power-law spectrum extends to at least 30 MHz, Baldwin 1971). The cooling energy is the same as for Component-I, equation (5). Thus, Component-II is in the slowly cooling regime ($\epsilon_{\rm c} \geq \epsilon_{\rm p}$).

In addition, Component-II has an intrinsic injection break at the minimal energy of Component-I. In this case ,

$$
\nu F_\nu \propto
\begin{cases}
\epsilon^{4/3} & \epsilon < \epsilon_{\mathrm{p,II}} \\
\epsilon^{(3-p_{\mathrm{II}})/2} = \epsilon^{0.7} & \epsilon_{\mathrm{p,II}} < \epsilon < \epsilon_{\mathrm{c}} \\
\epsilon^{(2-p_{\mathrm{II}})/2} = \epsilon^{0.2} & \epsilon_{\mathrm{c}} < \epsilon < \epsilon_{\mathrm{p,I}} \\
\epsilon^{(2-p_{\mathrm{II,above}})/2} = (\text{steeper than})\epsilon^{-0} & \epsilon_{\mathrm{p,I}} < \epsilon \\
e^{-\epsilon/\epsilon_{\mathrm{s}}} & \epsilon_{\mathrm{s}} < \epsilon, \ \epsilon_{\mathrm{s}} \sim 100 \mathrm{MeV}
\end{cases}
\tag{14}
$$

with $p_{\mathrm{II}} = 1.6$ and $p_{\mathrm{II,\,above}} > 2$

4.3.2 Component-II: energetics

The luminosity of Component-II at the cooling break is $\nu F_\nu \sim 10^{-8}$ erg cm^2 s^{-1}, see Fig. 1 (it grows slowly above the cooling break). So, the present total luminosity of Component-II is $L_{\mathrm{p,\,II}} \sim 5 \times 10^{36}$ erg s^{-1}, well below the spin-down luminosity (this estimate may increase due to a possible rise of Component-II towards the optical). The total energetics of Component-II for a distance of 2 kpc and age of 1000 yr is $\sim 10^{48}$ erg. This is a considerable fraction (few per cent at least) of the total energy of the magnetohydrodynamic (MHD) flow (Kennel & Coroniti 1984a). Since, in the IR, electrons are in a marginally cooled state, this is also the estimate of the total energetics in the particles contributing to Component-II. It is safely below the power that the pulsar put into the Nebula during its life time, regardless of the initial spin.

In other words, assume that Component-II continues without a break up to the injection energy of Component-I, 1 eV, but only the 0.01–1 keV part is in the fast cooling regime. In a magnetic field b_0, the corresponding Lorentz factors are $\gamma_{\mathrm{p}} \approx 5 \times 10^5$ and $\gamma_{\mathrm{c}} \approx 5 \times 10^4$. Neglecting for simplicity, the energy of Component-II above the break, the relative amount of energy deposited into the fast cooling part of Component-II is then $1 - (\gamma_{\mathrm{c}}/\gamma_{\mathrm{p}})^{2-p_{\mathrm{II}}} \approx 0.6$ for $p_{\mathrm{II}} = 1.6$. Thus, approximately half of the energy transferred from the magnetic field to the particles in the reconnection events (Component-II) is given to the slowly cooling particles.

Thus, Component-II dissipates a considerable fraction of the Poynting luminosity of the wind (and most of the magnetic flux). A large fraction of the injected energy remains in the form of the turbulent magnetic field, plus approximately half of the dissipated energy is given to the slowly cooling particles. We thus conclude that the overall energetic requirement on Component-II are consistent with observations.

The fact that the energetics of Component-II is a non-negligible fraction of the total energy put into the Nebula by the pulsar is expected on theoretical grounds – in order to resolve the sigma-paradox, a considerable fraction of the spin-down luminosity should be dissipated (Lyutikov 2006; Porth, Komissarov & Keppens 2013). (As a cautionary note, what is needed to resolve the sigma-paradox is the destruction of the large scale magnetic flux, not magnetic energy; Lyutikov 2006.)

Thus, the energetics of Component-II is very reasonable – a large fraction of the energy that the pulsar puts into the Nebula in a form of mostly Poynting flux is dissipated in reconnection events within the turbulent medium. On the other hand, the problem of the number of radio electrons remains, provided they are supplied by the wind (Atoyan 1999b; Komissarov 2013). For the number distribution $\mathrm{d}n/\mathrm{d}\gamma = C\gamma^{-p_{\mathrm{II}}}$, and assuming that the distribution extends to at least the cooling break, the total number of electrons

within Component-II can be estimated as

$$
N_{\mathrm{II}} \approx \frac{L_{\mathrm{p,II}}\tau}{m_{\mathrm{e}}c^2}\gamma_{\mathrm{c}}^{-2+p_{\mathrm{II}}}\gamma_{\mathrm{min,II}}^{1-p_{\mathrm{II}}} = \frac{L_{\mathrm{p,II}}\tau}{m_{\mathrm{e}}c^2}\gamma_{\mathrm{c}}^{-0.4}\gamma_{\mathrm{min,II}}^{-0.6}
$$
$$
= 4 \times 10^{51} b_0^{0.8}\gamma_{\mathrm{min,II}}^{-0.6}.
\tag{15}
$$

Comparing with the injection rate

$$
\dot{N} = \lambda \frac{\Omega B_{\mathrm{NS}}}{2\pi e c}\pi R_{\mathrm{NS}}^2 \frac{\Omega R_{\mathrm{NS}}}{c}c
\tag{16}
$$

the needed multiplicity is

$$
\lambda = 2 \times 10^7 b_0^{0.8}\gamma_{\mathrm{min}}^{-0.6}.
\tag{17}
$$

The allowed $\gamma_{\mathrm{min}} \geq 100$, which would still require $\lambda \geq 10^6$. This is $\sim$ two orders of magnitude higher than the models of pulsar magnetospheres predict (e.g. Arons & Scharlemann 1979; Timokhin 2010).

4.3.3 Can Component-II extend to GeV energies?

Synchrotron spectra of accelerated particles may generally have two cut-offs – the synchrotron limit (de Jager et al. 1996; Lyutikov 2010) and possibly a potential limit within the acceleration region. The synchrotron limit (independent of magnetic field) is given by equation (1).

The total electric potential drop with the Nebula corresponds to the maximal Lorentz factor

$$
\gamma_{\mathrm{tot}} \sim \frac{e\sqrt{L_{\mathrm{sd}}}}{m_{\mathrm{e}}c^{5/2}} = 7 \times 10^{10}
\tag{18}
$$

where $L_{\mathrm{sd}} = 4 \times 10^{38}$ erg s^{-1} is the spin-down power. It is hard/nearly impossible for particles, especially leptons, to gain the full potential (Bell 1992, discussed how cosmic rays with large Larmor radius can achieve the potential drop).

If a particle gains a fraction η_{p} of the maximal potential (18), then in a given magnetic field particles will produce synchrotron photons with energy

$$
\epsilon_{\mathrm{tot}} \approx \hbar\eta_{\mathrm{p}}^2\gamma_{\mathrm{max}}^2\omega_{\mathrm{B}} = \frac{e^3\hbar B L_{\mathrm{sd}}}{m_{\mathrm{e}}^3 c^6} = 20\,\mathrm{GeV}\,b_0\,\eta_{\mathrm{p}}^2
\tag{19}
$$

Thus, to reach the synchrotron limit (1), a particle needs to cross ~ 0.05 of the total potential (Lyutikov et al. 2018).

The example of Crab flares demonstrates that under certain conditions particles do achieve the synchrotron limit (1). Thus, there are acceleration sites that can, at least occasionally, gain large overall potentials, with $\eta_{\mathrm{p}} \sim 0.1$. This implies that there is no intrinsic limit on η_{p} (that is, there is no requirement from observations to have an intrinsic limit on the possible accelerating potential – there is no limit on η_{p}, besides $\eta_{\mathrm{p}} < 1$).

One can then imagine a (power-law) distribution of reconnection sites with different total electric potential drops $\eta_{\mathrm{p}} < 1$, with no special value for η_{p}. The overall spectrum is then a combination of intrinsic p (that may also depend on the distribution of σ_{w}), distribution of γ_{max}, and how many particles are accelerated in a sheet with given γ_{max}.

4.3.4 Dominance of Component-II in radio

Scalings (6) and (14) naturally explain why Component-II dominates in radio – below the cooling frequency [globally in the IR, equation (5), but locally at higher frequencies] Component-I sharply drops off (as $\epsilon^{4/3}$ in νF_ν) and becomes subdominant to

Component-II. Component-I dominates in the optical, UV and X-rays (Component-II experiences a cooling break, while Component-I increases toward the injection break). Thus, in our model, it is a natural consequence that the X-ray bright Component-I becomes subdominant below the cooling frequency (locally in the 'torus' around 0.1 eV, and globally around 0.01 eV).

4.3.5 *Explanation of the possible MeV bump/requirement of the spectral break in Component-II*

Above the injection break Component-I is slowly decreasing with $\nu F_\nu \propto \epsilon^{1-p_I/2} \approx \epsilon^{-0.1}$, while below the injection break Component-I has globally $\nu F_\nu \propto \epsilon^{1/2}$. In the torus, $\nu F_\nu \propto \epsilon^{4/3}$ (in the torus particles did not have time to cool to form $\epsilon^{1/2}$ tail). The Component-II above the cooling break is slowly increasing with $\nu F_\nu \propto \epsilon^{1-p_{II}/2} \approx \epsilon^{0.2}$. Thus, Component-II may start to dominate over Component-I. Parametrizing spectral fluxes as:

Component-I:

$$F_I = F_{I,0} \left(\frac{\epsilon_p}{\epsilon_c}\right)^{-1/2} \left(\frac{\epsilon}{\epsilon_p}\right)^{-\alpha_I} \tag{20}$$

where $F_{I,0}$ is the spectral flux of Component-I at the cooling energy ϵ_c; above ϵ_c the spectral flux first increases $\propto \epsilon^{1/2}$, and then decays as $\epsilon^{-\alpha_I}$.

Component-II:

$$F_{II} = F_{II,0} \left(\frac{\epsilon}{\epsilon_p}\right)^{-\alpha_{II}-1/2} \tag{21}$$

where $F_{II,0}$ is the spectral flux of Component-II at the cooling energy, α_{II} is the uncooled spectral index, and factor 1/2 in the spectral exponent accounts for the spectral break.

The two components become equal at

$$\epsilon \sim \left(\frac{F_{I,0}}{F_{II,0}}\right)^{2/(2(\alpha_I+\alpha_{II})-1)} \epsilon_p^{(1+2\alpha_I)/(2(\alpha_I+\alpha_{II})-1)} \epsilon_c^{-2(1-\alpha_I)/(2(\alpha_I+\alpha_{II})-1)}$$

$$\approx \left(\frac{F_{I,0}}{F_{II,0}}\right)^{3.3} \frac{\epsilon_p^2}{\epsilon_c} = 200\,\text{eV} \left(\frac{F_{I,0}}{F_{II,0}}\right)^{3.3} b_0^5 \tag{22}$$

This is clearly not seen, yet the ratio of the intensities in the X-ray band is a sensitive function of both the overall normalization and, especially, of the local magnetic field, $\propto b_0^5$. The ratio (22) can easily extend beyond hundreds of keV for $F_{I,0}/F_{II,0} \sim$ few and $b_0 \sim$ few. It is tempting to associate the possible COMPTEL MeV bump (Section 2.2) with re-emergence of Component-II.

Alternatively, in order not to overshoot Component-I in the X-rays Component-II should experience a mild spectral break somewhere between IR and hard X-rays. As we argue in Section 5.2.5 one might expect injection the break in Component-II corresponding to the average energy per particle, γ_p, which is the $\gamma_{I<\min}$.

4.3.6 *Component-II: acceleration sites*

In our model, Component-II is accelerated in the bulk of the Nebula, but still in the central parts, see Fig. 7. There are several arguments in favour of centrally concentrated acceleration of Component-II, as opposed to evenly distributed over the Nebula: (i) the spectrum of Component-II requires regions with high magnetization, $\sigma \gg 1$ – see Section 5.2.5. Such regions do exist in the central parts of the Nebula, see Fig. 7; and (ii) spectral evolution in the IR towards the

edges of the Nebula (Fig. 2), requires that particles are centrally accelerated, and that turbulence is not effective in mixing particles with different ages.

Even though radio emitting electrons (Component-II) are accelerated now in intermittent reconnection events, we do not expect any kind of scintillation over the radio nebula – radio electrons are very inefficient radiators, so an addition of freshly accelerated leptons to large pool of already present ones will not produce much of an enhancement, see Sections 4.2.2.

5 ORIGIN OF COMPONENT-I AND COMPONENT-II

Next, we discuss a physical origin for Component-I and Component-II. Briefly, both components are supplied by the pulsar: the equatorial section of the termination shock accelerates Component-I, higher latitudes of the shock just thermalize the flow, while Component-II is given by particles that are accelerated in the turbulence that self-consistently generates reconnecting current sheets in the bulk of the Nebula.

5.1 Component-I: the wind termination shock

5.1.1 *Component-I: insights from MHD simulations*

The overall properties of the Crab X-ray emission are well reproduced by numerical models that assume low-sigma, equatorially dominated flow (Komissarov & Lyubarsky 2004). In addition, modelling of the Inner Knot (Lyutikov et al. 2016; Yuan & Blandford 2015) requires that the magnetization of the section of the pulsar wind producing the knot is low, $\sigma_w \leq 1$. Thus, the agreement of X-ray observation and low-sigma numerical models require that the equatorial part of the wind must have low magnetization, $\sigma_w \ll 1$. The requirement of a low-magnetized equatorial part sides nicely with the results of PIC modelling of Fermi-I acceleration in a weakly magnetized pair plasma, see Section 5.1.2. Thus, low-sigma MHD models and results of PIC simulations require/reproduce the Crab X-ray torus.

5.1.2 *Component-I: insights from PIC simulations*

Component-I is attributed to systematic Fermi-I acceleration at the relativistic shock that terminates the pulsar wind. In pulsar winds, if the rotational and magnetic axes of the central pulsar are misaligned, the wind around the equatorial plane consists of toroidal stripes of alternating magnetic polarity, separated by current sheets of hot plasma. Such a 'striped wedge' extends at latitudes $\lambda \leq \xi$, where $\xi = \arccos(\hat{\mu} \cdot \hat{\Omega})$ is the angle between magnetic and rotational axes of the pulsar (i.e. the pulsar inclination angle). For higher latitudes, the wind carries a non-alternating magnetic field.

Assuming that the stripes survive until the termination shock (Lyubarsky & Kirk 2001; Kirk & Skjæraasen 2003, but see Cerutti & Philippov 2017), we now describe the physics of particle acceleration if the pre-shock flow carries a strong magnetic field of intensity B_0, oriented perpendicular to the shock normal and alternating with wavelength $\ell = c\,P$, where P is the pulsar period. For the Crab Nebula, we assume that the pre-shock (before the alternating stripes get annihilated) Lorentz factor of the wind is $\gamma_w \sim 100$, and the pre-shock magnetization is $\sigma_w = B_0^2/(4\pi\gamma_w\rho_0 c^2) \sim 3 \times 10^3$ (here, B_0 and ρ_0 are the wind magnetic field and mass density as measured in the frame of the nebula). Importantly, if the magnetic energy is completely transferred to the particles (either in the wind or at the
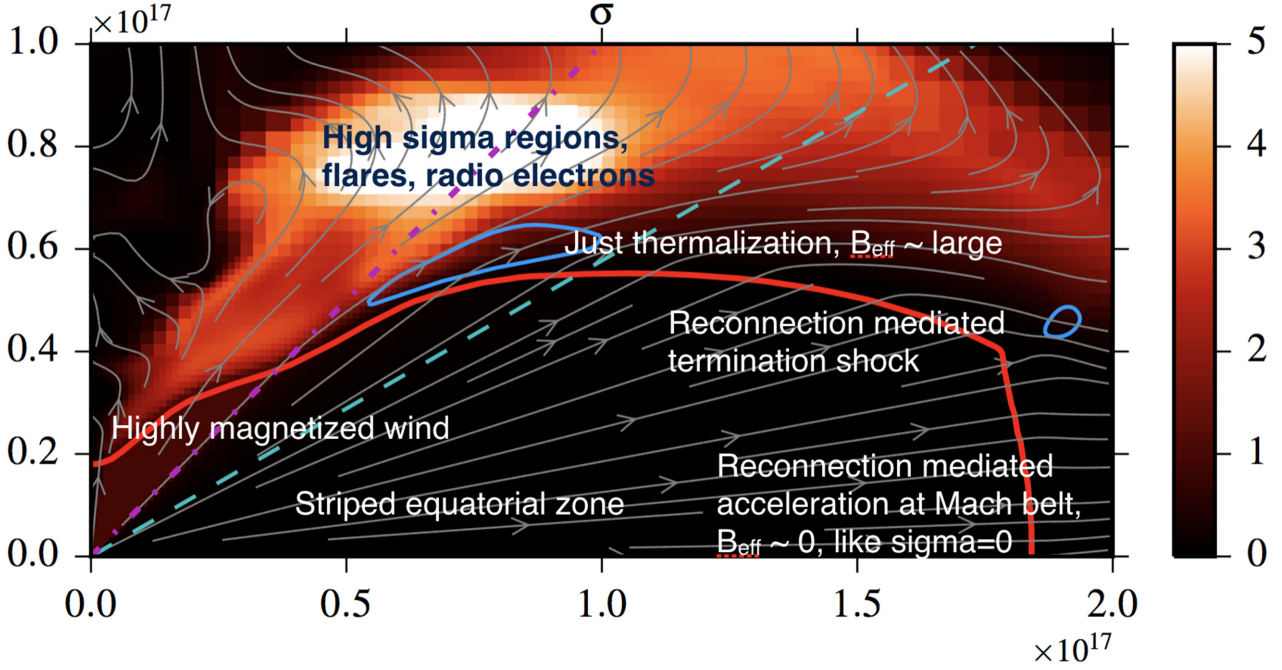
Figure 7. Magnetization σ_w and instantaneous streamlines near the termination shock in RMHD simulations of the Crab Nebula (Porth et al. 2014). The dotted–dashed straight line shows the separation of the polar and striped zones of the pulsar wind. The dashed straight line is the line of sight. The solid red line shows the termination shock and the solid blue loop between the dashed and dotted–dashed lines shows the region of Doppler-beamed emission associated with the inner knot of the Nebula. The polar beam corresponds to the streamlines originating from the inner part of the termination shock located to the left of the intersection with the dotted–dashed line. We added notations describing various properties of the wind/acceleration regions.

shock), the mean particle Lorentz factor increases from γ_w up to

$$\gamma_p = \gamma_w \sigma_w. \tag{23}$$

Although the magnetic field strength in the wind is always B_0, the wavelength-averaged field $\langle B_\phi \rangle_\ell$ can vary from zero up to B_0, depending on the relative widths of the regions of positive and negative field. In pulsar winds, one expects $\langle B_\phi \rangle_\ell = 0$ only in the equatorial plane (where the stripes are symmetric), whereas $|\langle B_\phi \rangle_\ell|/B_0 \to 1$ at high latitudes (more specifically, at latitudes $\lambda \to \xi$). As a proxy for latitude, we choose $\alpha_\ell = 2\langle B_\phi \rangle_\ell/(B_0 + |\langle B_\phi \rangle_\ell|)$, which varies between zero (at the midplane) and unity (at $\lambda = \xi$). We now describe the expected shape of the particle spectrum as a function of α_ℓ (or equivalently, latitude), assuming that both γ_w and σ_w are independent of latitude. Our arguments are motivated by the results of PIC simulations described in Sironi & Spitkovsky (2011a).

At the termination shock, the compression of the flow forces the annihilation of nearby field lines through driven magnetic reconnection (Lyubarsky 2003; Sironi & Spitkovsky 2011b, 2012). The efficiency of field dissipation is a function of latitude. Taking $\langle \gamma \rangle/\gamma_w \gtrsim 0.8$ as a criterion for efficient dissipation, we find that for $\alpha_\ell \lesssim 0.5$ most of the magnetic energy is dissipated, and as a result of reconnection the mean particle Lorentz factor increases from $\sim\gamma_w$ up to $\gamma_p \sim \gamma_w\sigma_w$. The resulting shape of the reconnection-powered particle spectrum depends on the ratio $\ell/r_{L,hot}$, where $r_{L,hot} = \sqrt{\sigma_w}\,c/\omega_p$ (being ω_p the plasma frequency), namely the stripe wavelength measured in units of the post-shock particle Larmor radius (i.e. after dissipation has taken place, and the mean particle energy has increased by a factor of σ_w). For Crab parameters, this ratio is small, and the resulting reconnection-powered particle spectrum should resemble a broad Maxwellian peaking at $\sim\gamma_w\sigma_w$ (Sironi & Spitkovsky 2011b). A Maxwellian peaking at

$\sim\gamma_w\sigma_w$ lying in a region with low residual magnetization is indeed invoked to explain the radiation spectrum of the Inner Knot.

At higher latitudes ($\alpha_\ell \gtrsim 0.5$), only a moderate or minor fraction of the incoming field energy is dissipated. For $0.5 \lesssim \alpha_\ell < 1$, the post-shock particle spectrum consists of two Maxwellian components. The low-energy peak comes from cold plasma with mean Lorentz factor $\sim\gamma_w$, whereas the high-energy part is populated by hot particles that gained energy from field dissipation, so that their mean Lorentz factor is now $\sim\gamma_w\sigma_w$. With increasing latitude, the high-energy part gets depopulated at the expense of the low-energy part. For $\lambda \geq \xi$, i.e. at latitudes beyond the striped wedge, only the low-energy part peaking at $\sim\gamma_w$ survives. Here, the magnetic energy per particle is still large. Further downstream, in the bulk of the nebula, turbulent dissipation of the dominant magnetic energy embedded in this portion of the wind will give rise to Component-II.

As we have just discussed, on most of the shock surface, shock-driven reconnection is not expected to produce non-thermal particle distributions. Rather, depending on the latitude, in the immediate post-shock region one expects a Maxwellian peaking at $\sim\gamma_w$ or at $\sim\gamma_w\sigma_w$ (or a combination of the two). We do not expect to see a simple thermal bump in the integrated spectrum, though. The oblique post-shock flow has a large spread in Lorentz factors, and a corresponding large spread in the internal temperatures (Komissarov & Lyutikov 2011). Also, these leptons were at the lower end of the injection spectrum $\gamma_{min,I} \sim \gamma_p$, and on the time-scale of the Nebula they cooled-off into the optical. Variations in B-field and the spread in post-shock temperatures (for oblique shocks) can erase a simple thermal distribution.

The equatorial wedge at $\alpha_\ell \lesssim 0.03 - 0.1$ represents an exception – here a systematic Fermi process can efficiently operate, in analogy to what happens in weakly magnetized shocks. Since the stripes are quasi-symmetric, the highest energy particles accelerated by

the reconnection electric field can escape ahead of the shock, and be injected into a Fermi-I acceleration cycle by 'surfing' the alternating magnetic fields (effectively, the shock in the equatorial plane has zero stripe-averaged field, and it displays the same acceleration capabilities of a weakly magnetized or unmagnetized shock, Spitkovsky 2008; Sironi et al. 2013). In the post-shock spectrum, the shock-accelerated particles populate a power-law tail with slope $p \simeq 2.3$ that extends beyond the Maxwellian at $\gamma_w \sigma_w$ produced by reconnection. In summary, Component-I can be produced via Fermi-I acceleration in the equatorial region (at latitudes $\tan \lambda / \tan \xi \lesssim 0.03$–0.1): its minimum Lorentz factor is $\sim \gamma_w \sigma_w$, and the slope of the non-thermal tail is $p \simeq 2.3$.

5.2 Component-II: the turbulent nebula

5.2.1 Overview

We propose that magnetized turbulence generates reconnecting current sheets of different sizes in the bulk of the Nebula. Particles are then accelerated by magnetic reconnection in the current layers and by scattering-off turbulent fluctuations. We suggest that this is the origin of Component-II. For a distribution of reconnecting sheets, with different sizes, that accelerate particles to some spectral slope p, to different γ_{max} (determined by the size of the reconnection region and the inflow velocity), the final average spectrum will be a combination of intrinsic p, distribution of γ_{max}, and how many particles are accelerated in a sheet with given γ_{max}. In addition, reconnection regions may occur in environments with different σ_w – there will be scaling with the relative contribution of different regions. Finally, particles can be further accelerated by stochastic interactions with turbulent fluctuations, producing a nontermal tail that extends well beyond the energy gained via magnetic reconnection alone (Comisso & Sironi 2018).

There are requirements on the spectrum of Component-II that have to be kept into consideration. Radio electrons (the low-energy part of the distribution produced by Component-II) have $p_{II} \approx 1.6$ (for the Crab). Then, there will be a cooling break in the IR. On top of that, there should be another mild break, in order to extend the spectrum from radio to gamma-rays, see Fig. 6. The break may come from combination of particles accelerated in regions with different σ_w – if larger regions have on average smaller magnetization (which, in reconnection, leads to steeper slopes) then the higher energy part of the spectrum will be softer.

We expect that extra break of Component-II is related to the mean energy per particle. Thus, it is the same as $\gamma_{I, min}$ of the shock-accelerated Component-I (see below).

5.2.2 Component-II: the problem of $\gamma_{min, II}$

Kennel & Coroniti (1984a,b) recognized two important problems with the radio emitting electrons in the Crab: (i) the minimal Lorentz factor for radio emitting electrons, $\gamma_{min, II} \leq 100$, is well below the average energy per particle $\gamma_p \geq \sim 10^6$. It is expected that the termination shock heats particles to the Lorentz factor γ_p and further accelerates beyond that via Fermi-I process. Thus, Component-II requires $\gamma_{min, II}$ well below the expected average energy per particles in the wind.

We already outlined a possible resolution of $\gamma_{min, II}$ in Section 5.1.2. The pulsar wind is relativistic, $\gamma_w \gg 1$, and magnetically dominated, $\sigma_w \gg 1$. Thus, the total energy per particle (in terms of $m_e c^2$) is $\gamma_p \sim \gamma_w \sigma_w$. Within the striped part of the wind this total energy is given to the particles. We assume $\gamma_w \sim 10^2$ and $\sigma_w \sim 10^3$; thus, $\gamma_{min, I} \sim \gamma_p \sim 10^5$. At the intermediate attitudes, where

the wind is not striped, only the bulk energy is thermalized, giving $\gamma_{min, II} \sim \gamma_w \sim 10^2$.

5.2.3 Turbulence is required to resolve the σ-problem

Kennel & Coroniti (1984a) identify the so-called sigma-problem of pulsar winds: models of pulsar magnetospheres predict $\sigma_w \gg 1$, while such flows cannot be accommodated with the non-relativistically expanding nebula. Numerical simulations of the global structure of the Crab Nebula (Porth et al. 2014) observations of larger scale structure in radio (Dubner et al. 2017), as well as modelling of emission (Porth et al. 2016) demonstrate that the structure of the Crab Nebula is highly turbulent. This runs contrary to the Kennel & Coroniti (1984a) model that envisions smooth evolution of the flow and the magnetic field from the termination shock to the edges. Turbulent redistribution of the magnetic flux from large scales to small scales, accompanied by the dissipation of magnetic energy, is required to resolve the sigma-problem (Lyutikov 2006, 2010; Porth et al. 2013).

5.2.4 Very hard spectral indices in radio – not Fermi-I at shocks

The majority of PWNe have radio spectral indices $\alpha \sim 0.1$–0.2 (Green 2014). This implies a particle index $p \approx 1.2$. Such hard spectra are not expected from a Fermi-I shock process, which typically produces $p > 2$ (e.g. Blandford & Eichler 1987, and Section 5.1.2). On the other hand, reconnection in highly magnetized plasmas can produce spectra that approach $p \sim 1$: in two dimensions (Zenitani & Hoshino 2001, 2007; Jaroschek, Lesch & Treumann 2004; Bessho & Bhattacharjee 2005, 2007, 2010, 2012; Hesse & Zenitani 2007; Daughton & Karimabadi 2007; Lyubarsky & Liverts 2008; Cerutti et al. 2012b; Sironi & Spitkovsky 2014; Guo et al. 2014, 2015a; Liu et al. 2015; Nalewajko et al. 2015; Sironi, Petropoulou & Giannios 2015; Sironi, Giannios & Petropoulou 2016; Werner et al. 2016; Kagan, Nakar & Piran 2016, 2018; Petropoulou et al. 2019; Cerutti et al. 2014b; Lyutikov et al. 2017a; Lyutikov et al. 2018, 2017b; Cerutti et al. 2012a; Guo et al. 2015b;enitani & Hoshino 2008), and in three dimensions (Zenitani & Hoshino 2005, 2008; Yin et al. 2008; Liu et al. 2011; Sironi & Spitkovsky 2011b, 2012; Kagan, Milosavljević & Spitkovsky 2013; Cerutti et al. 2014c; Sironi & Spitkovsky 2014; Guo et al. 2015a; Werner & Uzdensky 2017). There is a clear trend: higher sigma plasmas produce harder spectra, seeming to approach $p \sim 1$ in the very high-sigma limit.

5.2.5 Component-II: insights from PIC simulations

The post-shock high-latitude flow has a small mean Lorentz factor γ_w, and most of the energy per particle still resides in the magnetic field. When transported through the nebula, the magnetic energy might be dissipated, as a result of reconnection in a turbulent environment. It is well known that reconnection in magnetically dominated pair plasmas can produce hard particle spectra (Zenitani & Hoshino 2001; Sironi & Spitkovsky 2014; Guo et al. 2014; Werner et al. 2016). Simulations of reconnection have shown that $p \lesssim 2$ for $\sigma_w \gtrsim 10$ (but see Petropoulou et al. 2019), and the slope tends asymptotically to $p \to 1$ in the limit $\sigma_w \gg 1$ appropriate for the Crab Nebula. However, it is conceivable to assume that the superposition of spectra from different regions in the nebula will soften the space-averaged electron spectrum of Component-II to the observed $p \approx 1.6$. It remains to be explored whether such a

superposition is a natural result of inhomogeneities in the structure of the nebula.

We thus envision that reconnection in the nebula can naturally give the hard spectrum required for the radio electrons, above $\sim \gamma_{\rm w}$. In simulations of $\sigma_w \gg 1$ reconnection of an isolated current sheet, the high-energy cut-off of the particle distribution evolves quickly up to $\gamma_{\rm max} \sim 4 \gamma_{\rm w} \sigma_{\rm w}$ (Werner et al. 2016), followed by a slower evolution to higher energies (Petropoulou et al. 2019). In a turbulent environment, one might argue that particles energized by reconnection to Lorentz factors $\gtrsim \gamma_{\rm p} = \gamma_{\rm w} \sigma_{\rm w}$ would be further accelerated by turbulent fluctuations (here, we neglect the factor of 4 between $\gamma_{\rm max}$ and $\gamma_{\rm p}$); in contrast, the particle spectrum between $\gamma_{\rm w}$ and $\sim \gamma_{\rm p}$ will be entirely determined by reconnection, since particles will be trapped in reconnection plasmoids and cannot be effectively scattered by turbulence.

Particle acceleration in a self-similar sequence of current sheets produced by a turbulent cascade has recently been investigated by Zhdankin et al. (2017) and Comisso & Sironi (2018). These works have demonstrated that the generation of a power-law particle energy spectrum extending beyond the mean energy per particle $\sim \gamma_{\rm w} \sigma_{\rm w}$ is a generic by-product of magnetized turbulence. More specifically, Comisso & Sironi (2018) have shown that in a magnetized turbulent environment where turbulence and reconnection interplay, particle injection from the thermal bath at $\gamma_{\rm w}$ up to $\sim \gamma_{\rm w} \sigma_{\rm w}$ is governed by the reconnection electric field; some particles are then further accelerated by stochastic interactions with turbulent fluctuations, producing a non-thermal tail extending much beyond the mean energy per particle. The power-law slope of the high-energy tail is harder for higher magnetizations and stronger turbulence levels. While the regime $\sigma_{\rm w} \gg 1$ appropriate for the Crab Nebula is yet to be fully explored, we find that the slope can become harder than $p = 2$ (Comisso & Sironi 2018), but it is in general steeper than the slope generated by reconnection alone with the same parameters.

We then argue that a break in the particle distribution of Component II should appear around $\gamma_{\rm p} \sim \gamma_{\rm w} \sigma_{\rm w}$ (this is also the location of the injection Lorentz factor for Component I): at lower energies, energization is controlled by reconnection; at higher energies, reconnection-injected particles are further accelerated by turbulence. We remark, though, that at this point this is merely an hypothesis motivated by the distinct roles of the two acceleration mechanisms, as discussed in Comisso & Sironi (2018). To assess the validity of this assumption, one will need simulations of turbulence with $\sigma_{\rm w} \gg 1$ and a large dynamic range between the energy-carrying turbulent scales and the Larmor radius of particles energized by reconnection.

In summary, we expect the particle spectrum of Component-II to be a broken power law: from $\sim \gamma_{\rm w}$ to $\sim \gamma_{\rm w} \sigma_{\rm w}$, the space-averaged spectrum has slope $p \approx 1.6$ (but it is locally expected to be as hard as $p = 1$), in response to acceleration via reconnection; beyond the break at $\sim \gamma_{\rm w} \sigma_{\rm w}$, particles are accelerated by a stochastic process akin to Fermi II, with a steeper slope $p \gtrsim 2$.

The time-scale of the stochastic acceleration process is comparable to that of magnetic reconnection in the strong turbulence scenario considered here. Indeed, in this regime, the energy diffusion coefficient is $D_{\gamma \gamma} \sim 0.1 \gamma^2 (c/l)$, as measured in Wong et al. (2019) and Comisso & Sironi (2018). Here, l indicates the integral scale of turbulence, which specifies the energy-containing scale, and is also indicative of the size of the longest current sheets in the turbulent environment. Therefore, the stochastic acceleration time-scale $t_{\rm acc} \sim \gamma^2 / D_{\gamma \gamma} \sim 10 l/c$ is fast and comparable to that of magnetic reconnection.

We expect that at the largest scales, the statistics of current sheets might not be described as a self-similar sequence controlled by turbulent motions. There could be non-self-similar current sheets that result from large-scale collisions of flux tubes (Lyutikov et al. 2017b). In this case, if $\sigma_{\rm w} \sim 10$–100, the reconnection might be responsible for particle acceleration up to the maximum available potential (for such magnetizations, $p \sim 2$, and the maximum particle energy is not constrained by the fixed energy content of the system). Particle acceleration at these large-scale current sheets, Component-II, can extend up to the synchrotron burn-off limit and beyond, thus powering the Crab Nebula gamma-ray flares (Lyutikov et al. 2017a, 2018)

6 DISCUSSION

In this paper, we advance a two-component model of the Crab Nebula broad-band synchrotron emission. Component-I arises from the shock acceleration at the equatorial part of the pulsar wind termination shock (and thermalization at higher latitudes), while Component-II is generated from the interplay between reconnection events and turbulent fluctuations in the bulk of the Nebula. We suggest that Component-II extends from radio to gamma-rays, but is subdominant to Component-I in the range from the optical band to hard X-rays. There are two independent motivations for the separate Component-II related to magnetic reconnection and turbulence: very hard radio spectra and gamma-ray flares – both are inconsistent with shock acceleration.

We envision the following structure/acceleration properties of the Crab PWN (Fig. 7):

(i) The Crab pulsar produces a relativistic highly magnetized wind.

(ii) The equatorial part of the termination shock, of the order of $\sim 10°$ around the equator, accelerates X-ray emitting particles via the reconnection-mediated Fermi-I mechanism, while at higher latitudes, the reconnection-mediated shock just thermalizes the wind. This produces Component-I with $\gamma_{\rm min, I} \sim \gamma_{\rm w} \sigma_{\rm w} \sim 10^5$.

(iii) Component-I is in the fast cooling regime on the time-scale of the Nebula. Cooled leptons produce optical and near-IR emission (with a spectral index close to $\alpha = 0.5$, steepening towards the edges).

(iv) At even higher latitudes, the termination shock thermalizes only the bulk energy of the wind, $\gamma_{\rm min, II} \sim \gamma_{\rm w} \sim 10^2$.

(v) Turbulence in high-sigma regions in the mid-to-high latitudes leads to the formation of reconnecting current sheets and turbulent fluctuations that accelerate particles from radio to $\sim$100 MeV. Rare large-scale reconnection events lead to Crab gamma-ray flares. Radio and gamma-ray flares are produced by the same population (Component-II), different from X-rays (Component-I).

(vi) The above-GeV photons are produced by IC scattering of the synchrotron emission, in a conventional way. Subdominant extension of the synchrotron emission of Component-II to MeV energies will not change appreciably the IC component which has been previously calculated using the observed synchrotron spectra (Atoyan & Aharonian 1996; Meyer et al. 2010; Martín, Torres & Rea 2012).

We interpret the UV peak in the spectrum of the Crab Nebula as arising from the peak injection of particles accelerated at the equatorial part of the termination shock with a power-law index $p_{\rm I} \approx 2.2$. The UV peak energy corresponds to the $\gamma_{\rm p} \sim \gamma_{\rm w} \sigma_{\rm w} \sim$ few $\times$ 10^5. Optical and near-IR photons are produced by cooled leptons, both those accelerated at the equatorial part of the termination shock

and those that are just thermalized at the shock at intermediate latitudes. This naturally produces spectral index $\sim$0.5.

Radio-emitting particles require injection index $p_{\mathrm{II}} \approx 1.6$, which is too hard for the Fermi-I acceleration. We suggest that radio emitting particles are accelerated in turbulence mediated reconnection events. Component-II experiences two breaks: a cooling break in the IR and an intrinsic injection break corresponding to the minimal Lorentz factor of Component-I. In the optical and UV Component-II is mostly overwhelmed by Component-I. The injection break in Component-II above the IR is needed for Component-II not to overshoot Component-I up to hard X-rays (if there were no break in Component-II, it would produce a slightly rising spectrum $\nu F_\nu \propto \nu^{0.2}$ above the cooling break, that may overshoot the falling $\nu F_\nu \propto \nu^{-0.1}$ of Component-I in the X-rays). We hypothesize that Component-II extends to the synchrotron burning-off limit of 100 MeV. In our model, magnetized turbulence with reconnecting current sheets accelerates both the radio electron and also produces the Crab γ-ray flares.

Importantly, the implied bulk Lorentz factor in the wind is fairly low, $\gamma_{\mathrm{w}} \sim 10^2$. Conventional models of particle acceleration near the polar caps (e.g. Arons & Scharlemann 1979) predict $\gamma_{\mathrm{w}} \sim 10^4$–$10^6$. On the other hand, there is still no complete kinetic model of pulsar magnetospheres that include pair production and particle acceleration self-consistently.

In the present model, the region $\sim$0.01–1 eV is the most complicated: this is where several competing effects contribute nearly equally: (i) this is where the overall cooling break is for both components ($\sim$0.01 eV); (ii) where the peak of Component-I is ($\sim$1 eV); and (iii) where Component-I cools into optical, 1eV $\rightarrow$ 0.1 eV. All these estimates are a strong function of local B-field, hence large variations are expected.

The model has several predictions:

(i) *Details of the spectrum of the torus: shape of the UV peak:* the shock-produced Component-I is in the fast cooling regime on the lifetime of the Nebula, but is in the slowly cooling regime on the life-time of particles in the torus (years). In our model, the UV peak is the injection break of Component-I. Thus, the spectrum of the torus should change from $\nu F_\nu \propto \nu^{4/3}$ below the peak to $\nu F_\nu \propto \nu^{(3-p_{\mathrm{I}})/2} \propto \nu^{0.4}$ (hence, it is a break not a peak). Only at higher frequencies should it steepen to $\nu F_\nu \propto \nu^{(2-p_{\mathrm{I}})/2} \propto \nu^{-0.1}$. (These are asymptotic estimates, for well-separated cooling, injection and the observed frequencies; more detailed computations are needed to address the shape of the UV bump.) There is another testable prediction of the model related to the UV peak. If higher latitudes only thermalize the flow, this may have an effect on the shape of the peak.

(ii) *Possible reappearance of Component-II above hard X-rays:* in the model, Component-II becomes subdominant to Component-I above the cooling break at $\sim$0.01 eV. It may also experience an injection break at $\gamma_{\mathrm{I, min}}$. Depending on the value of the spectral index $p_{\mathrm{II, above}}$ above the break, Component-II may eventually dominate over Component-I (which is slowly decreasing with frequency above the peak). The MeV COMPTEL bump, Section 2.2, offers tantalizing hints.

(iii) *Flares in the low MeV range:* in our model the MeV COMPTEL bump, Section 2.2, is interpreted as a different component from the lower energy X-rays; it extends to GeV energies and occasionally produces γ-ray flares. We may expect flares in the lower MeV range. Flares from Component-II also occur in the X-ray region, but at those energies, the integrated flux is dominated by Component-I, so that only the brightest X-ray flares could possibly be detectable.

(iv) We expect a Doppler-broadened thermal peak in the UV, corresponding to just thermalized wind component at high latitudes.

There are a number of issues that need to be addressed within the model, that we leave to the future study: a combined radiative model of the two synchrotron emitting components; (i) calculations of the SSC spectrum within the model (e.g. whether the spatially-dependent magnetic field of $\sim$500 μG is consistent with the IC signal; and (ii) calculations of the spectral evolution of Component-I (e.g. one would predict temporary hardening in optical as the peak particles from Component-I first cool into optical from the UV into optical and then into IR).

REFERENCES

Abdo A. A., Ackermann M., Ajello M., Allafort A., Baldini L., Ballet J., Barbiellini G., Bastieri D. E., 2011, Science, 331, 739
Abdo A. A. et al., 2010, ApJ, 708, 1254
Aharonian F. et al., 2006, A&A, 457, 899
Arons J., Scharlemann E. T., 1979, ApJ, 231, 854
Atoyan A. M., 1999a, A&A, 346, L49
Atoyan A. M., 1999b, A&A, 346, L49
Atoyan A. M., Aharonian F. A., 1996, MNRAS, 278, 525
Baldwin J. E., 1971, in Davies R. D., Graham-Smith F., eds, IAU Symp. Vol. 46, The Crab Nebula. Kluwer, Dordrecht, p. 22
Bandiera R., Neri R., Cesaroni R., 2002, A&A, 386, 1044
Bell A. R., 1992, MNRAS, 257, 493
Bessho N., Bhattacharjee A., 2005, Phys. Rev. Lett., 95, 245001
Bessho N., Bhattacharjee A., 2007, Phys. Plasmas, 14, 056503
Bessho N., Bhattacharjee A., 2010, Phys. Plasmas, 17, 102104
Bessho N., Bhattacharjee A., 2012, ApJ, 750, 129
Bietenholz M. F., Kassim N., Frail D. A., Perley R. A., Erickson W. C., Hajian A. R., 1997, ApJ, 490, 291
Blandford R., Eichler D., 1987, Phys. Rep., 154, 1
Bucciantini N., Arons J., Amato E., 2011, MNRAS, 410, 381
Camus N. F., Komissarov S. S., Bucciantini N., Hughes P. A., 2009, MNRAS, 400, 1241
Cerutti B., Philippov A. A., 2017, A&A, 607, A134
Cerutti B., Uzdensky D. A., Begelman M. C., 2012a, ApJ, 746, 148
Cerutti B., Werner G. R., Uzdensky D. A., Begelman M. C., 2012b, ApJ, 754, L33
Cerutti B., Werner G. R., Uzdensky D. A., Begelman M. C., 2013, ApJ, 770, 147
Cerutti B., Werner G. R., Uzdensky D. A., Begelman M. C., 2014a, Phys. Plasmas, 21, 056501
Cerutti B., Werner G. R., Uzdensky D. A., Begelman M. C., 2014b, ApJ, 782, 104

Cerutti B., Werner G. R., Uzdensky D. A., Begelman M. C., 2014c, ApJ, 782, 104

Clausen-Brown E., Lyutikov M., 2012, MNRAS, 426, 1374

Comisso L., Sironi L., 2018, Phys. Rev. Lett., 121, 255101

Daughton W., Karimabadi H., 2007, Phys. Plasmas, 14, 072303

de Jager O. C., Harding A. K., Michelson P. F., Nel H. I., Nolan P. L., Sreekumar P., Thompson D. J., 1996, ApJ, 457, 253

Del Zanna L., Amato E., Bucciantini N., 2004, A&A, 421, 1063

Draine B. T., 1989, in Böhm-Vitense E., ed., ESA SP-290, Infrared Spectroscopy in Astronomy. ESA, Noordwijk

Dubner G., Castelletti G., Kargaltsev O., Pavlov G. G., Bietenholz M., Talavera A., 2017, ApJ, 840, 82

Gallant Y. A., Tuffs R. J., 2002, in Slane P. O., Gaensler B. M., eds, ASP Conf. Ser. Vol. 271, Neutron Stars in Supernova Remnants. Astron. Soc. Pac., San Francisco, p. 161

Green D. A., 2014, Bull. Astron. Soc. India, 42, 47

Guo F., Li H., Daughton W., Liu Y.-H., 2014, Phys. Rev. Lett., 113, 155005

Guo F., Liu Y.-H., Daughton W., Li H., 2015a, ApJ, 806, 167

Guo F., Liu Y.-H., Daughton W., Li H., 2015b, ApJ, 806, 167

Hesse M., Zenitani S., 2007, Phys. Plasmas, 14, 112102

Indebetouw R. et al., 2005, ApJ, 619, 931

Jaroschek C. H., Lesch H., Treumann R. A., 2004, ApJ, 605, L9

Jourdain E., Roques J. P., 2009, ApJ, 704, 17

Kagan D., Milosavljević M., Spitkovsky A., 2013, ApJ, 774, 41

Kagan D., Nakar E., Piran T., 2016, ApJ, 826, 221

Kagan D., Nakar E., Piran T., 2018, MNRAS, 476, 3902

Kennel C. F., Coroniti F. V., 1984a, ApJ, 283, 694

Kennel C. F., Coroniti F. V., 1984b, ApJ, 283, 710

Kirk J. G., Skjæraasen O., 2003, ApJ, 591, 366

Komissarov S. S., 2013, MNRAS, 428, 2459

Komissarov S. S., Lyubarsky Y. E., 2004, MNRAS, 349, 779

Komissarov S. S., Lyutikov M., 2011, MNRAS, 414, 2017

Kuiper L., Hermsen W., Cusumano G., Diehl R., Schönfelder V., Strong A., Bennett K., McConnell M. L., 2001, A&A, 378, 918

Lazarian A., Vishniac E. T., 1999, ApJ, 517, 700

Liu W., Li H., Yin L., Albright B. J., Bowers K. J., Liang E. P., 2011, Phys. Plasmas, 18, 052105

Liu Y.-H., Guo F., Daughton W., Li H., Hesse M., 2015, Phys. Rev. Lett., 114, 095002

Lyubarsky Y., Kirk J. G., 2001, ApJ, 547, 437

Lyubarsky Y., Liverts M., 2008, ApJ, 682, 1436

Lyubarsky Y. E., 2003, MNRAS, 345, 153

Lyutikov M., 2006, New J. Phys., 8, 119

Lyutikov M., 2010, MNRAS, 405, 1809

Lyutikov M., Komissarov S., Sironi L., 2018, J. Plasma Phys., 84, 635840201

Lyutikov M., Komissarov S. S., Porth O., 2016, MNRAS, 456, 286

Lyutikov M., Sironi L., Komissarov S. S., Porth O., 2017a, J. Plasma Phys., 83, 635830601

Lyutikov M., Sironi L., Komissarov S. S., Porth O., 2017b, J. Plasma Phys., 83, 635830602

Madsen K. K. et al., 2015, ApJ, 801, 66

Martín J., Torres D. F., Rea N., 2012, MNRAS, 427, 415

Meyer M., Horns D., Zechlin H.-S., 2010, A&A, 523, A2

Nalewajko K., Uzdensky D. A., Cerutti B., Werner G. R., Begelman M. C., 2015, ApJ, 815, 101

Olmi B., Del Zanna L., Amato E., Bandiera R., Bucciantini N., 2014, MNRAS, 438, 1518

Olmi B., Del Zanna L., Amato E., Bucciantini N., 2015, MNRAS, 449, 3149

Petropoulou M., Sironi L., Spitkovsky A., Giannios D., 2019, ApJ, 880, 37

Porth O., Buehler R., Olmi B., Komissarov S., Lamberts A., Amato E., Yuan Y., Rudy A., 2017, Space Sci. Rev., 207, 137

Porth O., Komissarov S. S., Keppens R., 2013, MNRAS, 431, L48

Porth O., Komissarov S. S., Keppens R., 2014, MNRAS, 438, 278

Porth O., Vorster M. J., Lyutikov M., Engelbrecht N. E., 2016, MNRAS, 460, 4135

Rees M. J., Gunn J. E., 1974, MNRAS, 167, 1

Reynolds S. P., 2001, Space Sci. Rev., 99, 177

Reynolds S. P., Pavlov G. G., Kargaltsev O., Klingler N., Renaud M., Mereghetti S., 2017, Space Sci. Rev., 207, 175

Rudy A. et al., 2015, ApJ, 811, 24

Sari R., Narayan R., Piran T., 1996, ApJ, 473, 204

Schweizer T., Bucciantini N., Idec W., Nilsson K., Tennant A., Weisskopf M. C., Zanin R., 2013, MNRAS, 433, 3325

Seward F. D., Tucker W. H., Fesen R. A., 2006, ApJ, 652, 1277

Sironi L., Giannios D., Petropoulou M., 2016, MNRAS, 462, 48

Sironi L., Petropoulou M., Giannios D., 2015, MNRAS, 450, 183

Sironi L., Spitkovsky A., 2011a, ApJ, 726, 75

Sironi L., Spitkovsky A., 2011b, ApJ, 741, 39

Sironi L., Spitkovsky A., 2012, Comput. Sci. Discov., 5, 014014

Sironi L., Spitkovsky A., 2014, ApJ, 783, L21

Sironi L., Spitkovsky A., Arons J., 2013, ApJ, 771, 54

Spitkovsky A., 2008, ApJ, 673, L39

Tang X., Chevalier R. A., 2012, ApJ, 752, 83

Tavani M. et al., 2011, Science, 331, 736

Temim T. et al., 2006, AJ, 132, 1610

Timokhin A. N., 2010, MNRAS, 408, 2092

van der Meulen R. D. et al., 1998, A&A, 330, 321

Veron-Cetty M. P., Woltjer L., 1993, A&A, 270, 370

Weisskopf M. C. et al., 2013, ApJ, 765, 56

Werner G. R., Uzdensky D. A., 2017, ApJ, 843, L27

Werner G. R., Uzdensky D. A., Cerutti B., Nalewajko K., Begelman M. C., 2016, ApJ, 816, L8

Willingale R., Aschenbach B., Griffiths R. G., Sembay S., Warwick R. S., Becker W., Abbey A. F., Bonnet-Bidaud J.-M., 2001, A&A, 365, L212

Wong K., Zhdankin V., Uzdensky D. A., Werner G. R., Begelman M. C., 2019, preprint (arXiv:1901.03439)

Yin L., Daughton W., Karimabadi H., Albright B. J., Bowers K. J., Margulies J., 2008, Phys. Rev. Lett., 101, 125001

Yuan Y., Blandford R. D., 2015, MNRAS, 454, 2754

Zanin R., 2017, in Torres D. F., ed., Astrophysics and Space Science Library Vol. 446, Modelling Pulsar Wind Nebulae. Springer-Verlag, Berlin, p. 101

Zenitani S., Hoshino M., 2001, ApJ, 562, L63

Zenitani S., Hoshino M., 2005, Phys. Rev. Lett., 95, 095001

Zenitani S., Hoshino M., 2007, ApJ, 670, 702

Zenitani S., Hoshino M., 2008, ApJ, 677, 530

Zhdankin V., Werner G. R., Uzdensky D. A., Begelman M. C., 2017, Phys. Rev. Lett., 118, 055103

This paper has been typeset from a TEX/LATEX file prepared by the author.